Special Issue: Innovations in Sustainable Fisheries, Marine Resources, and Food Systems for Food Security and Human Well-being

Digital Image Processing for Automated Bacterial Colony Counting: A Prigi Coastal Case Study

Indah Yanti[1*], Marjono[1], Antariksa[2] and Andi Kurniawan[3]

[1]Department of Mathematics, Faculty of Mathematics and Natural Sciences, Brawijaya University, Malang, Indonesia; [2]Department of Architecture, Faculty of Engineering, Brawijaya University, Malang, Indonesia; [3]Department of Fisheries and Marine Resources Management, Faculty of Fisheries and Marine Sciences, Brawijaya University, Malang, Indonesia.

Abstract | Accurate colony enumeration is important for microbiological assessment, but manual plate counting is time-consuming and can vary among observers. This study evaluated an image-processing pipeline that combines fractional-order Perona-Malik anisotropic diffusion, morphological enhancement, and marker-controlled watershed segmentation. The evaluation used 18 images: 15 annotated public images and three images from a Prigi coastal case study. Each image was processed at ten fractional orders from 0.1 to 1.0 under the same requested diffusion settings, with an order-dependent cap on the Euler time step. In the public test subset, order 0.3 produced the lowest mean absolute error (22.00 colonies), whereas order 0.2 gave a similar mean absolute error (22.40 colonies) and the lowest root-mean-square error (41.76 colonies). The Friedman test indicated an overall effect of fractional order ($p = 0.0017$), although none of the 45 pairwise comparisons remained significant after Holm correction. Two test images were markedly overcounted throughout the sweep. In the three Prigi images, mean absolute error ranged from 7.00 to 30.00 colonies, with the minimum occurring at a different order from the public-subset minimum. These results suggest that fractional order should be interpreted as one component of the complete segmentation pipeline rather than as a transferable optimum. Given the small field subset and the persistent failure cases, the method is best regarded as a counting aid that still requires visual verification.

Received | April 04, 2026; **Accepted** | October 09, 2026; **Published** | November 28, 2026
***Correspondence** | Indah Yanti, Department of Mathematics, Faculty of Mathematics and Natural Sciences, Brawijaya University, Malang, Indonesia; **Email:** indah_yanti@ub.ac.id
Citation | Yanti, I., Marjono, Antariksa and A. Kurniawan. 2026. Digital image processing for automated bacterial colony counting: A prigi coastal case study. *Sarhad Journal of Agriculture,* 42(s2): 49-60.
DOI | https://dx.doi.org/10.17582/journal.sja/2026/42.s2.49.60
Keywords | Automated colony counting, Bacterial colonies, Coastal microbiology, Digital image processing, Fractional Perona–Malik diffusion, Image segmentation

Copyright: 2026 by the authors. Licensee ResearchersLinks Ltd, England, UK.
This article is an open access article distributed under the terms and conditions of the Creative Commons Attribution (CC BY) license (https://creativecommons.org/licenses/by/4.0/).

Introduction

Coastal monitoring depends on measurements that are both reproducible and interpretable. Anthropogenic pressures remain an important concern in Indonesian coastal waters, where the need for further research on biological contamination has also been identified (Adyasari *et al.*, 2021). Culture-based colony counts remain one practical component of microbiological assessment. Their usefulness, however, depends on a clear counting procedure and an explicit account of counting error. Manual plate enumeration is laborious and may be influenced by operator-dependent counting decisions,

particularly when colony boundaries are difficult to distinguish (Brugger *et al*., 2012; Hogekamp *et al*., 2020). Image-based analysis can make the enumeration step more reproducible, but a colony count alone does not establish the microbiological quality or safety of the original water sample.

Classical automated colony counters usually combine background correction, thresholding, connected-component analysis, and a procedure for separating touching colonies (Zhang *et al*., 2008; Brugger *et al*., 2012). OpenCFU, for example, evaluates candidate objects across several thresholds and uses a distance-transform watershed to split merged regions (Geissmann, 2013). These approaches are relevant here because plate illumination, agar colour, colony size, and colony shape can vary considerably from image to image. A single threshold or a fixed object-size rule is therefore unlikely to be reliable across all plates.

Perona-Malik anisotropic diffusion controls smoothing through a gradient-dependent conductivity function, allowing noise reduction while limiting diffusion across strong edges (Perona and Malik, 1990). Fractional calculus extends this idea by permitting non-integer spatial operators with a broader spatial response (Podlubny, 1999; Kilbas *et al*., 2006; Samko *et al*., 1993). Fractional anisotropic diffusion has been studied for image denoising and texture preservation (Bai and Feng, 2007; Yao *et al*., 2019; Shan *et al*., 2022). Those studies motivate the use of a fractional operator, but denoising performance cannot be assumed to translate directly into accurate colony enumeration; the complete enhancement-segmentation-counting pipeline has to be evaluated at the counting stage.

Learning-based methods provide another route to automated colony analysis, while publicly annotated plate images make systematic evaluation possible (Makrai *et al*., 2023; Solymosi and Nagy, 2023). Density-map approaches have also shown that colony number can be estimated without relying only on individually segmented objects (Graczyk *et al*., 2022). The present study follows a different strategy: no classifier or segmentation network is trained. Instead, the study documents the implemented fractional operator, examines counting error across a prespecified order grid, and assesses the applicability of the same rule-based pipeline to a small set of Prigi field images.

Materials and Methods

Biological material and evaluation images

The bacterial strain used was an indigenous *Pseudomonas aeruginosa* isolate originating from the Prigi Archipelago Fishing Port area, Trenggalek Regency, East Java Province, Indonesia. Culture maintenance and preparation were carried out in the Fisheries Product Safety Laboratory, Faculty of Fisheries and Marine Sciences, Universitas Brawijaya, Indonesia. The field evaluation comprised three culture images (indi01, 01_9288, and 01_9317) with reference counts of 97, 202, and 228 colonies, respectively.

The available image records did not permit reconstruction of how many independent environmental samples or culture plates were represented by these three files. The original isolation, culture, and image-acquisition settings were also not documented in enough detail for an acquisition-level reproducibility analysis. For this reason, the three Prigi images are reported as a descriptive case series and are not treated as three demonstrated independent biological replicates.

The public test subset contained 15 annotated images from the Figshare dataset of Solymosi and Nagy (2023). The corresponding data descriptor documents the wider collection and its annotation procedure (Makrai *et al*., 2023). Only the 15 images listed in Table 1 were used in the present analysis, with reference counts ranging from 27 to 450 colonies. Together with the three Prigi images, the study therefore evaluated 18 distinct images. Running every image at ten fractional orders produced 180 image-configuration records; these records are repeated configurations of 18 images, not 180 independent samples. Public and field results were consequently summarized separately.

No classifier or neural network was fitted. For each run, candidate segmentations were ranked from image-derived properties and internal consistency measures without using the reference count. The fractional-order sweep was exploratory and no separate development subset was available for choosing a final operating order. Accordingly, the lowest observed error is reported as a descriptive result of this sweep, not as an unbiased estimate of a tuned model's future performance.

Image preprocessing and region-of-interest detection

The workflow consists of region-of-interest detection, image enhancement using fractional-order anisotropic diffusion, adaptive segmentation, colony separation using a watershed algorithm, and quantitative evaluation. Figure 1 shows this sequence. Images were read in grayscale at their stored resolution. A median filter with a 7-pixel kernel was used for circle detection, rather than as a replacement for the input to the diffusion stage.

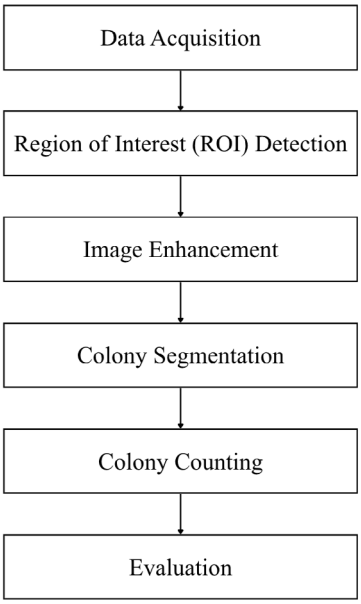

Figure 1: *Research methodology framework for the colony separation and counting algorithm.*

The Petri dish was located with a circular Hough transform. Candidate radii lay between 0.25 and 0.55 times the shorter image dimension. The detector used an inverse resolution ratio of 1.2, an edge threshold of 100, and an accumulator threshold of 35. Candidate circles were ranked by their distance from the image centre and deviation from a radius of 0.45 times the shorter image dimension. The selected radius was multiplied by 0.90 to reduce inclusion of the dish rim. If detection failed, a centred circle with radius 0.45 times the shorter image dimension was used.

Pixels outside the circular region of interest were filled with the median intensity inside it. Additional inward margins of 0%, 1%, 2%, or 3% of the region-of-interest radius were evaluated during segmentation. The term region-of-interest margin fraction refers to this additional relative erosion; it does not mean that half of the image or half of the mask was removed.

Implemented fractional Perona–Malik diffusion

The fractional spatial operator was constructed from the Grünwald–Letnikov definition (Podlubny, 1999; Kilbas *et al.*, 2006; Samko *et al.*, 1993) using two-sided, finite-memory differences. Let u denote the grayscale image, h the pixel spacing, M the memory length, and m the binary region-of-interest indicator. Coordinate indices 1 and 2 denote the horizontal and vertical directions. The side index s is L or R, with displacement signs sigma_L = -1 and sigma_R = 1, respectively. With reflected sampling at the image boundary, the directional differences were written as follows:

$$D^{\alpha}_{\ell,s}u(\mathbf{p}) = h^{-\alpha}\sum_{k=0}^{M}\widetilde{w}_k\; u(\mathbf{p}+\sigma_s k\mathbf{e}_\ell), \qquad \ell \in \{1,2\}.$$

The generalized binomial coefficients in the Grünwald–Letnikov stencil were evaluated recursively following the standard fractional-difference construction (Podlubny, 1999; Kilbas *et al.*, 2006). Truncating the memory causes the finite set of coefficients to have a nonzero sum, so an implementation-specific constant-response correction was introduced by adjusting only the central coefficient:

$$w_0 = 1, \quad w_k = -w_{k-1}\frac{\alpha-k+1}{k}, \quad \widetilde{w}_0 = w_0 - \sum_{k=0}^{M} w_k, \quad \widetilde{w}_k = w_k\ (k \geq 1).$$

This correction changes only the central coefficient; the remaining fractional weights are left unchanged. In all experiments, M = 12 and h = 1 pixel. The four directional responses defined a common gradient magnitude. The unmasked exponential Perona-Malik conductivity follows Perona and Malik (1990), and the implemented conductivity was restricted to the ROI by multiplication with the binary mask m:

$$s_n^2 = \tfrac{1}{2}\textstyle\sum_{\ell=1}^{2}\left[\left(D^{\alpha}_{\ell,L}u^n\right)^2 + \left(D^{\alpha}_{\ell,R}u^n\right)^2\right], \qquad c_0^n = \exp\left[-\left(\frac{s_n}{\kappa}\right)^2\right], \qquad c^n = mc_0^n.$$

The conductivity parameter was fixed at kappa = 25. Left- and right-sided fractional responses were then combined direction by direction. Finite Grünwald–Letnikov stencils of this type are commonly used in fractional diffusion discretizations (Yao *et al.*, 2019; Shan *et al.*, 2022), although the exact two-sided composition below is specific to the present implementation:

$$L_{\alpha,c^n}u^n = \frac{1}{2}\sum_{\ell=1}^{2}\left(D^{\alpha}_{\ell,R}\left(c^n D^{\alpha}_{\ell,L}u^n\right) + D^{\alpha}_{\ell,L}\left(c^n D^{\alpha}_{\ell,R}u^n\right)\right).$$

The image was advanced with 15 explicit Euler updates, consistent with the explicit time-marching strategy used in fractional diffusion solvers (Shan *et al*., 2022):

$$u^{n+1} = \mathrm{clip}_{[-64,319]}\left(u^n - \gamma_{\mathrm{eff}}\, mL_{\alpha,c^n} u^n\right).$$

The explicit Euler form follows the cited numerical strategy, whereas the intermediate clipping bounds in Eq. (5) are implementation-specific guard values. After the fifteenth update, image intensities were clipped to 0–255 and converted to 8-bit values. Boundary reflection did not repeat the edge pixel. The requested Euler step was 0.15. To limit excessively large explicit updates when the corrected coefficient norm increased, the following implementation-specific step cap was used:

$$\gamma_{\mathrm{eff}} = \min\left(\gamma_{\mathrm{requested}}, \frac{0.15}{\max(\| \widetilde{\mathbf{w}} \|_1^2, 10^{-8})}\right).$$

The same cap was applied at every order. It is a numerical safeguard used in this implementation, not a general stability theorem for every nonlinear, masked configuration. For the same reason, the operator is described here as a two-sided truncated Grünwald–Letnikov construction rather than as an exact rotationally invariant Riesz derivative.

Fractional order was varied from 0.1 to 1.0 in increments of 0.1. Table 2 reports the effective Euler step associated with each order. Because the coefficient norm changes with order, the applied step and the accumulated discrete diffusion time also change even though the requested step and the number of iterations are fixed. The experiment therefore measures sensitivity of the complete step-limited implementation. The 1.0 setting is the integer-order case of this discrete construction; it is not a separately tuned conventional Perona-Malik baseline.

Enhancement, segmentation, and watershed selection

Diffusion output was normalized within the region of interest using a median- and median-absolute-deviation-based scaling followed by clipping at the 0.5th and 99.5th percentiles. The resulting intensities were mapped to 0–255. Both bright-object white top-hat enhancement and dark-object black-hat enhancement were considered. Elliptical kernel diameters were the odd integers obtained from 3.5%, 5.5%, and 7.5% of the region-of-interest radius, with a minimum of 31 pixels.

Candidate binary masks were generated either by Otsu's histogram-based threshold (Otsu, 1979) or by the 97.0th, 97.5th, 98.0th, 98.5th, 99.0th, and 99.3rd intensity percentiles. Percentiles were calculated only from pixels inside the current region of interest. Otsu thresholding was applied to the enhanced image and then restricted to that region. Morphological choices were: no opening or closing, closing with a 3-pixel kernel, or opening followed by closing with 3-pixel kernels. Eight-connected components were used for mask statistics.

A typical colony area was estimated from conservative masks across both enhancement polarities and several kernel sizes. Median component areas were combined after rejecting poorly filled and elongated components. This estimate supplied a scale prior for removing small isolated components and penalizing fragmentation. The scoring function also penalized implausible foreground fractions, border occupancy, and abrupt count changes between neighbouring percentile thresholds. A component-density reference of 220 per million region-of-interest pixels was used as a soft penalty, not as a hard limit on the final count. Such rules are morphological assumptions and can still reject true colonies or accept noncolony structures.

The eight masks with the lowest mask scores were carried forward. After removal of small components, a Euclidean distance transform was smoothed with a Gaussian standard deviation of 0.8 pixels. Local maxima were identified using elliptical kernels of 3, 5, 7, or 9 pixels and relative peak thresholds of 0.08, 0.12, 0.16, 0.20, 0.24, or 0.30 of the maximum smoothed distance. Any connected component without a seed was assigned a marker at its distance maximum. Marker-controlled watershed segmentation was then applied to the inverse-distance surface following the standard watershed principle described by Vincent and Soille (1991).

The relative distance-peak threshold determines how high a peak must be before it becomes a watershed marker. It is distinct from the minimum accepted object area, which controls whether a segmented object is retained. The minimum area was calculated from the estimated colony scale and constrained to 3–80 pixels; the maximum area was the largest of 400

pixels, 18 times the estimated colony area, and 4% of the current region-of-interest area.

Each retained mask generated 24 combinations of peak threshold and peak-kernel size. Positive candidate counts were compared with the median count obtained from the same mask. Here, {N_r} denotes the positive candidate counts for that mask, N_j is the count for candidate j, and MAD is their median absolute deviation. The exact scoring expression below was defined for this study; its components reflect the multi-threshold and morphology-consistency rationale used in classical colony-counting pipelines (Brugger *et al.*, 2012; Geissmann, 2013):

$$S_j = S_{\text{mask}} + S_{\text{watershed},j} + 8\frac{\text{MAD}(\{N_r\})}{\max(\text{median}(\{N_r\}),1)} + 4\frac{|N_j - \text{median}(\{N_r\})|}{\max(\text{median}(\{N_r\}),1)}.$$

A consensus count was obtained as the median of the 12 candidates with the lowest total scores. The final candidate was the one whose count was closest to that consensus, with the total score used only to break ties. Reference counts were not used in this selection. Nevertheless, changing fractional order can change the enhanced image and thereby move an image to a different threshold, morphology, or watershed branch.

Counting metrics and statistical analysis

Let G_i denote the reference count and P_i the predicted count for image i. All reference counts in this study were positive. Signed error, absolute error, and absolute percentage error were calculated using the usual count-error definitions (Hyndman and Koehler, 2006):

$$e_i = P_i - G_i, \qquad AE_i = |e_i|, \qquad APE_i = 100\frac{|e_i|}{G_i}.$$

The original implementation also returned a quantity labelled 'accuracy'. To make this quantity reproducible and to avoid confusing it with classification accuracy, it is defined explicitly here as the following study-specific clipped relative counting score:

$$\text{Accuracy}_i = \min\left(100, \max\left(0, 100\left(1 - \frac{|P_i - G_i|}{G_i}\right)\right)\right), \qquad G_i > 0.$$

This quantity is not classification accuracy. Values were averaged across images for dataset-level summaries. When the absolute error is at least as large as the reference count, the score is clipped at zero, so increasingly large overcounts receive the same zero score. Mean absolute percentage error was therefore reported alongside it without clipping. The principal absolute-error summaries were calculated as follows (Hyndman and Koehler, 2006):

$$\text{MAE} = \frac{1}{n}\sum_{i=1}^{n}|e_i|, \qquad \text{RMSE} = \sqrt{\frac{1}{n}\sum_{i=1}^{n}e_i^2}.$$

Signed bias and mean absolute percentage error were computed as follows (Hyndman and Koehler, 2006):

$$\text{Bias} = \frac{1}{n}\sum_{i=1}^{n}e_i, \qquad \text{MAPE} = \frac{100}{n}\sum_{i=1}^{n}\frac{|e_i|}{G_i}.$$

Positive bias indicates overcounting and negative bias indicates undercounting. The proportion of images with an absolute error no greater than 10% of the reference count was used only as a descriptive tolerance summary; it is not presented as a microbiological acceptance criterion. Public test results and Prigi field results were not pooled when drawing the main conclusions.

Because the same 15 public images were evaluated at all ten orders, absolute errors were analysed as paired repeated measurements. The overall comparison used the Friedman rank test (Friedman, 1937), with Kendall's coefficient of concordance W reported as an effect-size summary (Kendall and Babington Smith, 1939). Pairwise comparisons used the Wilcoxon signed-rank statistic (Wilcoxon, 1945); for the exact calculations, sign assignments of the nonzero paired differences were enumerated and tied absolute differences received average ranks. Familywise multiplicity across all 45 order pairs was controlled with the Holm procedure (Holm, 1979). Nine contrasts against order 0.8 were retained as a clearly labelled exploratory comparison family. The significance level was 0.05.

Pointwise 95% percentile bootstrap intervals for test-set mean absolute error were obtained from 100,000 resamples of whole images (Efron, 1979). Each resampled image carried all ten order configurations together so that the paired structure was preserved. The resampling seed was 20260921. These intervals, like the rank tests, treat images as the independent analysis units; the available metadata were insufficient to establish biological independence among the source plates. No inferential test was applied to the three Prigi images.

Processing time was recorded separately for region-of-interest preparation, fractional diffusion with normalization, candidate and watershed search, and final labelling. The total timer included image reading but stopped before output files were written. Each image-order configuration supplied one timing observation. Hardware details and repeated timing trials were not available, so the timing summaries were treated as descriptive profiles rather than comparative speed benchmarks.

Results

Test-image counting performance

All 18 images were processed at each of the ten fractional orders. Circle detection returned a region of interest for every image. The recorded radius ranged from 977 to 1332 pixels for the test images and from 1008 to 1377 pixels for the field images. Circle-detection success does not, on its own, establish that every colony was included in the mask.

Selected orders for each public test image are summarized in Table 1. The smallest test-set mean absolute error was 22.00 colonies at order 0.3. Order 0.2 was nearly identical by this measure (22.40 colonies) and gave the lowest root-mean-square error, 41.76 colonies. The difference in mean absolute error between orders 0.2 and 0.3 was only 0.40 colonies. Eleven of the 15 images were within 10% of their reference count at order 0.2, compared with ten at order 0.3. For this dataset, the most defensible interpretation is therefore a low-error neighbourhood around 0.2–0.3 rather than a uniquely optimal order.

Predicted values are colony counts per image. Order 0.3 is shown in detail because it gave the lowest descriptive test-set mean absolute error in the sweep; it was not selected using an independent development set.

The full public-image sweep is reported in Table 2. Signed bias was positive at every order, indicating an overall tendency toward overcounting. At order 0.3, the mean clipped counting score was 81.86%, while mean absolute percentage error was 30.23%; the difference reflects the clipping built into the score. The 95% bootstrap interval for mean absolute error was 6.20–42.40 colonies at order 0.3 and 6.80–41.87 colonies at order 0.2.

Persistent failures and order-sensitive cases

Two public images remained clear failure cases across the entire order sweep. For sp16_img08 (reference count 32), predictions ranged from 119 to 130; for sp22_img04 (reference count 178), they ranged from 300 to 333 (Figure 2). At order 0.3, these two images contributed 218 colonies of absolute error, or 66.06% of the total test-set absolute error. Varying fractional order alone therefore did not correct these failures.

Table 1: *Per-image test counts for selected fractional orders. All ten configurations are reported in Supplementary Table S1.*

Image ID	Reference count	Predicted 0.2	Predicted 0.3	Absolute error, 0.3	Predicted 0.8	Predicted 1.0
sp06_img17	143	133	135	8	134	162
sp06_img07	128	127	129	1	136	134
sp12_img05	44	43	45	1	129	82
sp16_img08	32	119	122	90	128	129
sp16_img13	221	228	232	11	261	260
sp19_img03	106	144	130	24	162	145
sp19_img10	111	155	153	42	166	165
sp21_img06	27	28	30	3	27	27
sp21_img07	42	42	42	0	43	43
sp21_img13	61	57	58	3	57	57
sp21_img47	450	442	444	6	451	447
sp22_img04	178	300	306	128	311	316
sp22_img06	193	184	184	9	320	320
sp24_img11	90	87	88	2	87	86
sp24_img16	107	106	109	2	109	108

Table 2: *Test-image sensitivity and effective Euler steps (n = 15 images at each order).*

Order	Effective step	MAE	RMSE	Bias	Mean clipped counting score (%)	MAPE (%)
0.1	0.15000	28.53	51.77	+24.27	77.83	35.92
0.2	0.15000	22.40	41.76	+17.47	81.45	30.01
0.3	0.09224	22.00	42.55	+18.27	81.86	30.23
0.4	0.06597	33.67	54.99	+31.13	71.44	42.54
0.5	0.05330	39.93	61.55	+37.27	66.88	49.29
0.6	0.04635	40.53	63.46	+38.27	67.71	51.91
0.7	0.04228	38.67	59.15	+36.00	68.77	48.43
0.8	0.03983	41.33	62.29	+39.20	67.47	52.07
0.9	0.03835	39.07	59.78	+36.40	67.33	45.59
1.0	0.03750	38.00	59.12	+36.53	68.95	44.59

MAE, RMSE, and bias are in colonies. Requested step = 0.15; iterations = 15; memory length = 12; conductivity parameter = 25; pixel spacing = 1. All rows use the same requested settings and selection rules.

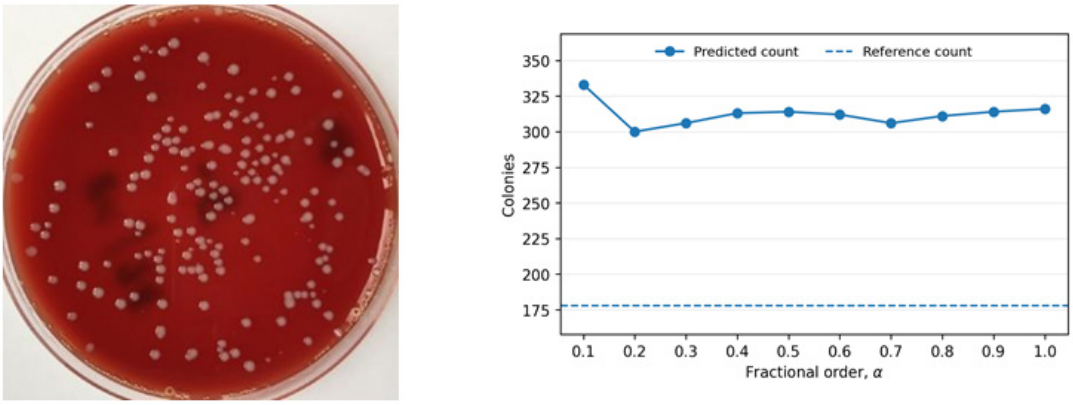

Figure 2: *Persistent overcounting in sp22_img04. (a) Original colour image. (b) Predicted counts across the fractional-order Perona-Malik anisotropic diffusion sweep; the dashed line is the reference count of 178.*

Order sensitivity was more abrupt in sp12_img05 and sp22_img06. From order 0.3 to 0.4, the prediction for sp12_img05 rose from 45 to 95 while the selected enhancement polarity switched from bright to dark. Over the same change in order, sp22_img06 rose from 184 to 305 colonies and the selected top-hat kernel changed from 87 to 41 pixels. The discontinuities therefore coincided with changes in the selected processing branch, although the present experiment cannot assign the change to a single stage in isolation. The two order-sensitive images accounted for 69.66% of the decrease in total absolute error between orders 0.8 and 0.3. In contrast, the most populated test image, sp21_img47, had a reference count of 450 and predictions between 442 and 451 over the entire sweep (Figure 3). Large reference counts were therefore not sufficient to explain the observed errors. Object-level matching would be needed to distinguish missed colonies, false positives, and excessive splitting.

Prigi field-image results

The three Prigi images showed a different order-response pattern (Table 3). Their lowest mean absolute

Table 3: *Counts and descriptive performance on the three Prigi field images.*

Order	indi 01 G =97	01_ 9288 G = 202	01_9 31 7G =228	MAE	RMSE	Mean clipped counting score (%)
0.1	106	202	216	7.00	8.66	95.15
0.2	103	153	193	30.00	34.94	84.74
0.3	106	159	190	30.00	33.54	84.26
0.4	106	163	198	26.00	28.88	86.09
0.5	105	165	205	22.67	25.57	87.78
0.6	110	170	214	19.67	21.52	88.21
0.7	108	173	217	17.00	19.00	89.83
0.8	107	177	230	12.33	15.59	92.15
0.9	106	182	236	12.33	13.48	92.44
1.0	106	176	231	12.67	15.98	92.18

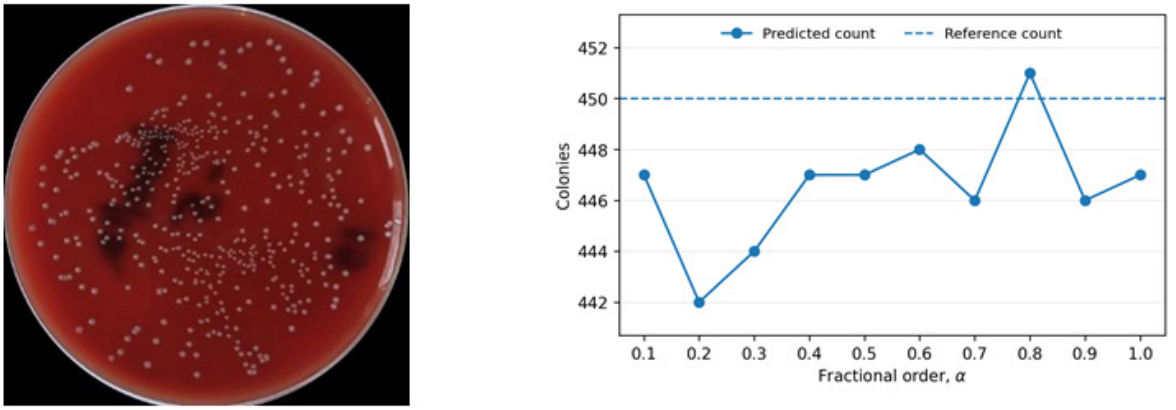

Figure 3: *Counting response for the high-count image sp21_img47. (a) Original colour image. (b) Predicted counts across the fractional-order Perona-Malik anisotropic diffusion sweep; the dashed line is the reference count of 450.*

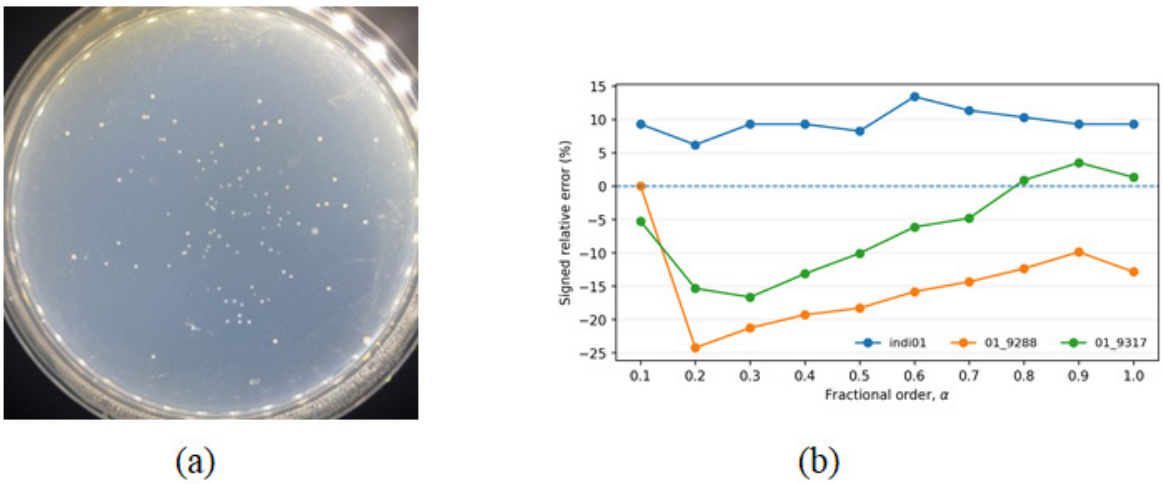

Figure 4: *Prigi field-image evaluation. (a) Representative Prigi culture photograph. (b) Signed relative counting error for indi01, 01_9288, and 01_9317 across the fractional-order Perona-Malik diffusion sweep. Zero indicates agreement with the reference count; positive values indicate overcounting and negative values indicate undercounting.*

error was 7.00 colonies at order 0.1, whereas orders 0.2 and 0.3 both produced the largest mean absolute error, 30.00 colonies. At order 0.1, predicted counts for indi01, 01_9288, and 01_9317 were 106, 202, and 216, compared with reference counts of 97, 202, and 228. All three counts were within 10% of their respective references at that order. Orders 0.8 and 0.9 each yielded a mean absolute error of 12.33 colonies.

G is the reference count. Errors are measured in colonies. No statistical inference or final parameter selection was made from this three-image subset.

indi01 changed little across the sweep, with predictions between 103 and 110, whereas 01_9288 varied from 153 to 202. Figure 4 shows signed relative error for all three Prigi images. The minimum at order 0.1 should not be interpreted as a field-specific recommendation because it was identified from only three images in the same exploratory sweep.

Fractional-order sensitivity and paired comparisons

Figure 5 shows the mean absolute error curves for the public and Prigi subsets separately. For the 15 public images, the Friedman test statistic was 26.5547 with nine degrees of freedom ($p = 0.0016567$; Kendall's $W = 0.1967$). The global result indicates that absolute-error ranks were not identical across the ten orders, although the size and direction of the response differed among images.

No individual order pair remained significant after Holm correction over all 45 comparisons. The unadjusted exact signed-rank p-value for orders 0.2 and 0.3 was 0.8984, consistent with their very similar mean absolute errors. Table 4 shows the separate

exploratory contrasts against order 0.8. For order 0.3 versus 0.8, absolute error was lower in 12 images, higher in two, and unchanged in one; the exact p-value was 0.007690 and the Holm-adjusted value within this nine-comparison exploratory family was 0.069214. Thus, the global Friedman result does not identify a single order as uniquely superior.

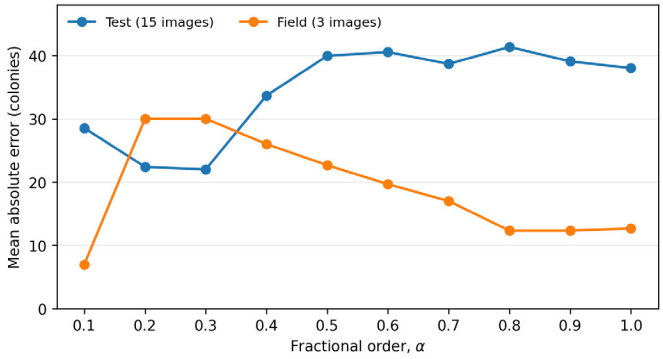

Figure 5: *Mean absolute counting error across the ten evaluated fractional orders. Public test images (n = 15) and Prigi field images (n = 3) are shown separately; the field curve is descriptive only.*

Table 4: *Exploratory paired absolute-error contrasts against order 0.8 on the test images.*

Order	Mean difference in absolute error	Lower / higher / equal error	Exact p-value	Holm-adjusted p-value (9 contrasts)
0.1	-12.80	7/5/3	0.451660	1.000000
0.2	-18.93	10/3/2	0.011230	0.089844
0.3	-19.33	12/2/1	0.007690	0.069214
0.4	-7.67	10/3/2	0.021484	0.150391
0.5	-1.40	7/6/2	0.405518	1.000000
0.6	-0.80	8/4/3	0.412109	1.000000
0.7	-2.67	7/5/3	0.191895	1.000000
0.9	-2.27	6/5/4	0.776367	1.000000
1.0	-3.33	6/5/4	0.777344	1.000000

Negative mean differences favour the listed order. Holm-adjusted p-values in this table apply only to the nine exploratory contrasts. No pair was significant under the principal correction across all 45 order pairs. Mean test errors changed relatively little between orders 0.7 and 0.9, but this aggregate pattern did not imply image-level equivalence. For example, sp12_img05 changed from 129 predicted colonies at order 0.8 to 83 at order 0.9. The results provide no basis for treating order 0.8 as a generally stable or optimal operating point.

Table 5: *Recorded processing-time profile over 180 image-configuration records.*

Stage	Mean time (seconds)	Share of summed time (%)
Region-of-interest preparation	3.91	6.24
Fractional diffusion and normalization	3.25	5.19
Candidate and watershed search	55.51	88.54
Final labelling and count evaluation	0.02	0.03
Total recorded time	62.69	100.00

Processing-time profile

Across all 180 image-configuration records, mean recorded processing time was 62.69 seconds. Candidate evaluation and watershed search accounted for 88.54% of the summed time, whereas fractional diffusion with normalization accounted for 5.19% (Table 5). The principal computational cost in this implementation was therefore the downstream search. These observations do not establish that the method is faster than manual counting or another automated system.

Output-file writing is excluded. The shares are ratios of summed stage times to summed total time, not averages of per-image percentages. These records are not 180 independent biological observations or repeated timing trials of the same configuration.

Discussion

The failure pattern points to segmentation, rather than colony number alone, as the main practical limitation of the current pipeline. A densely populated plate could remain close to its reference count, while other plates were overcounted at every fractional order. Rule-based colony counters face the same general difficulty when dish boundaries, local texture, or merged structures remain plausible foreground objects after thresholding. Geissmann (2013) addressed this problem in OpenCFU by evaluating morphology across thresholds and applying distance-transform watershed separation. The present results are consistent with that type of failure, although aggregate counts alone cannot identify which structures were falsely detected in each image.

The multi-branch selection strategy was included for the same reason: a credible segmentation should not depend on one isolated threshold. Brugger *et al.*

(2012) combined top-hat background correction with geometric checks on connected colony groups, while OpenCFU used repeated morphological validation across thresholds (Geissmann, 2013). In the present pipeline, these ideas are extended with scale and stability penalties. The order-sensitive branch changes show the limitation of this approach, however. Several candidate segmentations can agree with one another and still share the same error, and a relatively small change in the enhanced image can cause a different processing branch to be selected.

Fractional diffusion should therefore be viewed as an image-conditioning mechanism, not as a guarantee of better enumeration. Bai and Feng (2007) showed that fractional anisotropic diffusion can improve denoising while preserving image structure, and Yao *et al*. (2019) developed a related model for texture images affected by multiplicative noise. Shan *et al*. (2022) further emphasized that the precise fractional formulation and its numerical approximation matter. These studies support the use of fractional operators for edge-aware smoothing, but their image-quality findings do not imply that the same order will minimize colony-count error after thresholding and watershed segmentation.

A second issue is that fractional order is coupled to the numerical step in the present implementation. The coefficient-norm cap reduces the effective Euler step at higher orders while the iteration count remains fixed. As a result, changing order also changes the accumulated discrete diffusion time. The observed sensitivity curve must therefore be interpreted as a property of the complete step-limited pipeline, rather than a pure one-factor experiment on fractional order. A cleaner ablation would hold the effective step or diffusion time constant and compare fractional and non-fractional variants under the same downstream segmentation search.

Count agreement also has an important limitation: false detections and missed colonies can offset one another. Reporting absolute and percentage errors helps describe the magnitude of disagreement, but it does not reveal detection precision, recall, or the location of failures. Graczyk *et al*. (2022) reached the counting problem from a density-map perspective and explicitly considered count calibration and uncertainty, illustrating the value of examining more than a single aggregate score. For the present rule-based method, object-level matching against validated colony annotations would be the next step for separating missed colonies, false positives, and over-splitting.

The public and Prigi subsets should not be interpreted as interchangeable validation sets. Makrai *et al*. (2023) describe substantial variation in species, culture media, imaging conditions, and colony density in the full public dataset, whereas this study used only 15 of those images. The three Prigi photographs add a useful local application example, but they do not establish transfer across sampling dates, culture batches, laboratories, or imaging protocols. Their different response to fractional order may reflect acquisition or biological differences; the available metadata do not allow those explanations to be separated. Stronger field validation would require documented independent samples and plates, a fixed image-acquisition protocol, and independently reviewed reference counts.

The absence of model training also does not make the pipeline computationally trivial. Most recorded processing time was spent evaluating segmentation candidates and watershed configurations rather than in the fractional diffusion step. Geissmann (2013) reported execution time under specified hardware and software conditions, but comparable hardware information and repeated timing trials were not available here. Accordingly, the present study does not claim a speed advantage over manual counting or other automated systems. At its present stage, the method is better positioned as an auditable counting aid: a user can inspect the segmented result and manually review plates whose counts appear unreliable.

Conclusions and Recommendations

The proposed pipeline combines a two-sided truncated Grünwald–Letnikov operator with Perona-Malik conductivity and image-driven selection of enhancement and watershed parameters. Its response to fractional order was non-monotonic and strongly image dependent. Orders 0.2–0.3 produced the lowest descriptive errors on the 15 public test images, but no pairwise comparison remained significant after correction across all order pairs. The three Prigi images showed a different sensitivity pattern and are too few to define a transferable operating order.

The analysis also identified two limitations that should guide further work: some images remained

poorly counted across the full order sweep, and the order comparison was coupled to an order-dependent effective Euler step. A subsequent study should use a separate development set, matched baseline and ablation experiments, and object-level review of false detections and missed colonies. Based on the available evidence, the pipeline should be used as an aid to colony enumeration with visual verification, not as a validated replacement for manual counting or for the broader microbiological assessment of coastal samples.

Acknowledgements

The authors gratefully acknowledge the financial support provided by the Faculty of Mathematics and Natural Sciences (FMIPA), Universitas Brawijaya, through the Research Grant Scheme 2025.

Novelty Statement

This study combines a finite-memory, step-limited fractional diffusion operator with image-driven selection of enhancement, thresholding, and watershed parameters for bacterial colony counting. Its main contribution is not a claim of a universally optimal fractional order, but a reproducible implementation and an image-level sensitivity analysis showing where the pipeline is stable, where the processing branch changes, and where counting errors persist.

Authors' Contribution

Indah Yanti: Investigation, data analysis, methodology, and original draft preparation.
Marjono: Supervision and manuscript review.
Antariksa: Investigation and manuscript review.
Andi Kurniawan: Data investigation, funding acquisition, and manuscript finalization.
All authors read and approved the final manuscript.

Generative AI and AI-assisted technology statement
The authors declare that no generative AI and AI assisted technology was used in the creation of this manuscript.

Conflict of interest
The authors have declared no conflict of interest.

References

Adyasari, D., M.A. Pratama, N.A. Teguh, A. Sabdaningsih, M.A. Kusumaningtyas, and N. Dimova. 2021. Anthropogenic impact on Indonesian coastal water and ecosystems: Current status and future opportunities. Marine Pollut. Bullet., 171: 112689. https://doi.org/10.1016/j.marpolbul.2021.112689.

Bai, J. and X.C. Feng. 2007. Fractional-order anisotropic diffusion for image denoising. IEEE Transactions on Image Process., 16(10): 2492-2502. https://doi.org/10.1109/TIP.2007.904971.

Brugger, S.D., C. Baumberger, M. Jost, W. Jenni, U. Brugger, and K. Mühlemann. 2012. Automated counting of bacterial colony forming units on agar plates. PLoS ONE., 7(3): e33695. https://doi.org/10.1371/journal.pone.0033695.

Efron, B. 1979. Bootstrap methods: Another look at the jackknife. Annal. Statist., 7(1): 1-26. https://doi.org/10.1214/aos/1176344552.

Friedman, M. 1937. The use of ranks to avoid the assumption of normality implicit in the analysis of variance. J. Americ. Statist. Associat., 32(200): 675-701. https://doi.org/10.1080/01621459.1937.10503522.

Geissmann, Q. 2013. OpenCFU, a new free and open-source software to count cell colonies and other circular objects. PLoS ONE., 8(2): e54072. https://doi.org/10.1371/journal.pone.0054072.

Graczyk, K.M., J. Pawłowski, S. Majchrowska, and T. Golan. 2022. Self-normalized density map (SNDM) for counting microbiological objects. Scient. Repor., 12: 10583. https://doi.org/10.1038/s41598-022-14879-3.

Hogekamp, L., S.H. Hogekamp, and M.R. Stahl. 2020. Experimental setup and image processing method for automatic enumeration of bacterial colonies on agar plates. PLoS ONE, 15(6): e0232869. https://doi.org/10.1371/journal.pone.0232869.

Holm, S. 1979. A simple sequentially rejective multiple test procedure. Scandinav. J. Statist., 6(2): 65-70. https://doi.org/10.2307/4615733.

Hyndman, R.J., and A.B. Koehler. 2006. Another look at measures of forecast accuracy. Int. J. Forecast., 22(4): 679-688. https://doi.org/10.1016/j.ijforecast.2006.03.001.

Kendall, M.G., and B. Babington Smith. 1939. The problem of m rankings. Annal. Mathem. Statist., 10(3): 275-287. https://doi.org/10.1214/aoms/1177732186.

Kilbas, A.A., H.M. Srivastava, and J.J. Trujillo. 2006. Theory and Applications of Fractional Differential Equations. Elsevier, Amsterdam.

Makrai, L., B. Fodróczy, S.Á. Nagy, P. Czeiszing, I. Csabai, G. Szita, and N. Solymosi. 2023. Annotated dataset for deep-learning-based bacterial colony detection. Scient. Data., 10: 497. https://doi.org/10.1038/s41597-023-02404-8.

Otsu, N. 1979. A threshold selection method from gray-level histograms. IEEE Transactions on Systems, Man, and Cybernet., 9(1): 62-66. https://doi.org/10.1109/TSMC.1979.4310076.

Perona, P. and J. Malik. 1990. Scale-space and edge detection using anisotropic diffusion. IEEE Transactions on Pattern Analy. Mach. Intelligen., 12(7): 629-639. https://doi.org/10.1109/34.56205.

Podlubny, I. 1999. Fractional Differential Equations. Academic Press, San Diego.

Samko, S.G., A.A. Kilbas, and O.I. Marichev. 1993. Fractional Integrals and Derivatives: Theory and Applications. Gordon and Breach, Yverdon.

Shan, X., J. Sun, Z. Guo, W. Yao, and Z. Zhou. 2022. Fractional-order diffusion model for multiplicative noise removal in texture-rich images and its fast explicit diffusion solving. BIT Numer. Mathemat., 62: 1319-1354. https://doi.org/10.1007/s10543-022-00913-3.

Solymosi, N. and S. Nagy. 2023. Annotated dataset for deep-learning-based bacterial colony detection. Figshare. Dataset. https://doi.org/10.6084/m9.figshare.22022540.v3.

Vincent, L. and P. Soille. 1991. Watersheds in digital spaces: An efficient algorithm based on immersion simulations. IEEE Transactions on Pattern Analysis and Machine Intelligence, 13(6): 583-598. https://doi.org/10.1109/34.87344.

Wilcoxon, F. 1945. Individual comparisons by ranking methods. Biomet. Bullet., 1(6): 80-83. https://doi.org/10.2307/3001968.

Yao, W., Z. Guo, J. Sun, B. Wu, and H. Gao. 2019. Multiplicative noise removal for texture images based on adaptive anisotropic fractional diffusion equations. SIAM J. Imag. Sci., 12(2): 839-873. https://doi.org/10.1137/18M1187192.

Zhang, C., W.B. Chen, W.L. Liu, and C.B. Chen. 2008. An automated bacterial colony counting system. In: 2008 IEEE International Conference on Sensor Networks, Ubiquitous, and Trustworthy Computing, pp. 233-240. IEEE. https://doi.org/10.1109/SUTC.2008.50.